

Electronic Supplementary Information for

**Ultra-high energy storage properties in lead-free multilayer ceramic capacitors *via*
multiscale optimization strategy**

Peiyao Zhao^{1,†}, Ziming Cai^{1,2†}, Lingling Chen¹, Longwen Wu³, Yu Huan⁴, Limin Guo⁵,
Longtu Li¹, Hong Wang^{6,*}, Xiaohui Wang^{1,*}

***Corresponding author. Email: wxh@mail.tinghua.edu.cn (X. W.);
wangh6@sustech.edu.cn (H. W.)**

[†]These authors contributed equally to this work.

This PDF file includes:

Materials and Methods

Figure S1 to S15

Table S1 to S4

References

Materials and Methods

Phase-field Breakdown Model: To analyze the mechanism for the enhanced breakdown strength caused by the chemical coating method, a scalar spatially and temporally dependent damage field $s(x, t)$ is introduced to characterize the breakdown process of the BTBZNT ceramic and BTBZNT@SiO₂ ceramics, respectively¹⁻³. The value of s varies from 1 to 0, representing the intact state and the fully damaged state, respectively. For any other intermediate state, the permittivity is interpolated by

$$\varepsilon(s) = \frac{\varepsilon_0}{f(s) + \eta}, \quad (\text{S1})$$

where $f(s) = 4s^3 - 3s^4$ and ε_0 is the initial permittivity, η is a small enough constant and sets to be 1E-4 during modeling. Breakdown happens if the process decreases the total potential energy of the system,

$$\Pi[s, \phi] = \int_{\Omega} [W_{\text{es}}(E, s) + W_{\text{d}}(s) + W_{\text{i}}(\nabla s)] dV, \quad (\text{S2})$$

where $W_{\text{es}}(E, s) = -\frac{\varepsilon}{2} E \cdot E$ is the complementary electrostatic energy per unit volume, $W_{\text{d}}(s) = W_{\text{c}}[1 - f(s)]$ is the breakdown energy function with W_{c} representing the critical density of electrostatic energy, $W_{\text{i}}(\nabla s) = \frac{\Gamma}{4} \nabla s \cdot \nabla s$ is the gradient energy term to regulate sharp phase boundaries. Notably, the material parameter Γ is approximately the breakdown energy. According to linear kinetic law: $\partial s / \partial t = -m \delta \Pi / \delta s$, the evolution equation for breakdown variable s can be obtained after substituting in detailed forms of the energy functions:

$$\frac{1}{m} \frac{\partial s}{\partial t} = \frac{\varepsilon'(s)}{2} \nabla \phi \cdot \nabla \phi + W_{\text{c}} f'(s) + \frac{\Gamma}{2} \nabla^2 s. \quad (\text{S3})$$

Here, mobility m is a material parameter that indicates the speed of breakdown propagation in dielectric ceramics. By normalizing all lengths by l , energy densities by

W_c , time by $l^2/m\Gamma$, and electric potential by $\sqrt{\Gamma/\epsilon_0}$, the final normalized governing equations for the electrical potential and the breakdown process of dimensionless form can be written as:

$$\bar{\nabla} \cdot \left[\frac{1}{f(s) + \eta} \bar{\nabla} \bar{\phi} \right] = 0, \quad (S4)$$

$$\frac{\partial s}{\partial \bar{t}} = - \frac{f'(s)}{2[f(s) + \eta]^2} \bar{\nabla} \bar{\phi} \cdot \bar{\nabla} \bar{\phi} + f'(s) + \frac{1}{2} \bar{\nabla}^2 s, \quad (S5)$$

in which the corresponding quantities are symbolized with over-bars. The dielectric breakdown behavior of the BTBZNT ceramic and BTBZNT@SIO2 ceramics can be simulated by implementing the normalized governing equations (S4) and (S5) into COMSOL Multiphysics platform. The $\epsilon_{\text{shell}}/\epsilon_{\text{core}}$ and $\Gamma_{\text{shell}}/\Gamma_{\text{core}}$ are set to be 1/100 and 10/1, where ϵ_{shell} , ϵ_{core} are the dielectric permittivity of shell and core part of BTBZNT@SiO₂ ceramic, and Γ_{shell} , Γ_{core} are the breakdown energy of shell and core part of BTBZNT@SiO₂ ceramic, respectively.

Charge Transport Model: The charge transport model is based on the bipolar charge injection, transport, and trapping in the dielectrics as well as recombination of opposite charges when subjected to electric fields. The model has been implemented to allow simulation of BTBZNT and BTBZNT@SiO₂ MLCC with 5 μm thickness dielectrics that is subdivided into elements across its thickness.⁴ Charge generation is assumed to be by Schottky injection at the interface with electrons injected at the cathode ($x = 0$) and holes at the anode ($x = d$), such that

$$J_e(0, t) = AT^2 \exp\left(-eW_{ei}/kT\right) \exp\left(e/kT \sqrt{eE(0, t)/4\pi\epsilon}\right), \quad (S6)$$

$$J_h(d, t) = AT^2 \exp\left(-eW_{hi}/kT\right) \exp\left(e/kT \sqrt{eE(d, t)/4\pi\epsilon}\right), \quad (S7)$$

where $J_e(0, t)$ and $J_h(d, t)$ are the injection current densities at the cathode and anode, respectively; $E(0, t)$ and $E(d, t)$ are the electric fields; A is the Richardson constant; T is the temperature; e is the elementary electronic charge; k is the Boltzmann constant; w_{ei} and w_{hi} are the Schottky barrier heights for electrons and holes injection; and ε is the permittivity of the dielectric. The Schottky barrier heights for BTBZNT MLCCs of 0.64 eV and BTBZNT@SiO₂ MLCCs of 0.76 eV were fitted by Schottky emission model, as shown in the Fig. S13.

Charge transportations within solid dielectrics are essentially governed by three basic equations.⁴⁻⁷ They describes the behavior of charge carriers through a time and space dependent total flux $J(x, t)$ and by neglecting diffusion.

1) Poission's equation:

$$\frac{\partial E(x, t)}{\partial x} = \frac{\rho(x, t)}{\varepsilon} \quad (\text{S8})$$

2) Transport equation:

$$J(x, t) = \mu n(x, t)E(x, t) \quad (\text{S9})$$

3) Continuity equation:

$$\frac{\partial n(x, t)}{\partial t} + \frac{\partial J(x, t)}{\partial x} = s \quad (\text{S10})$$

where E is the electric field, ρ is the net charge density, ε is the dielectric permittivity, J is the current density, μ is the mobility of carriers, n is the density of mobile species, s is the source term, x and t are spatial coordinate and time, respectively. The charge trapping and recombination contribute to the source term s as illustrated in Fig. S1. The electric field distortion and space charge distribution can be

calculated by implanting formulas S6 to S9 into COMSOL platform.

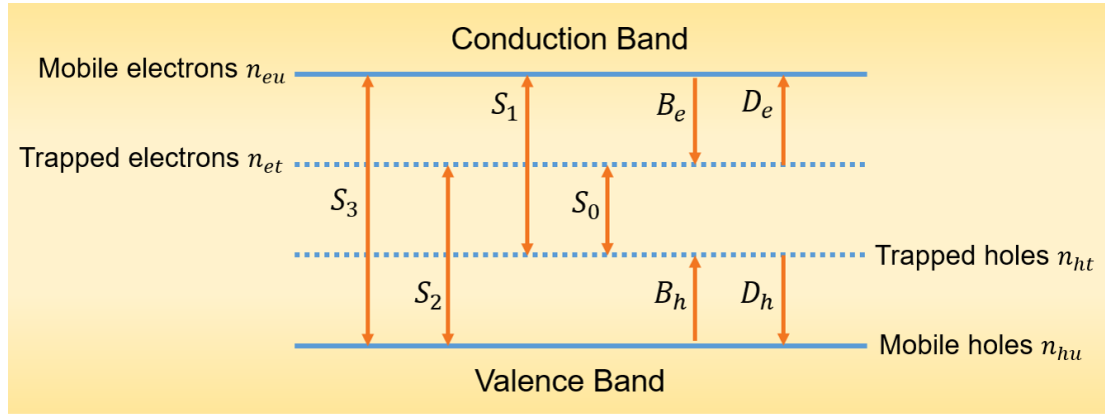


Figure S1 Schematic representation of the charge transport model. S_0 to S_3 are recombination coefficients, n_{eu} , n_{et} , n_{ht} , n_{hu} are mobile and trapped electron and hole densities. B_e and B_h are electron and hole trapping coefficients. D_e and D_h are electron and hole detrapping coefficients.

Material and Multilayer Energy Storage Ceramic Capacitors Fabrication: The $0.87\text{BaTiO}_3\text{-}0.13\text{Bi}(\text{Zn}_{2/3}(\text{Nb}_{0.85}\text{Ta}_{0.15})_{1/3})\text{O}_3$ (BTBZNT) powders were fabricated by a conventional solid-state reaction method. High-purity BaCO_3 , TiO_2 , Bi_2O_3 , ZnO , Nb_2O_5 , and Ta_2O_5 powders were mixed at designed stoichiometric ratios, ball milled for 24 hours and then calcined at $900\text{ }^\circ\text{C}$ for 4 hours in a closed alumina crucible. The calcined powders were ball milled again with 6 wt% poly(acrylic acid-co-maleic anhydride) as surfactant to obtain the well-dispersed slurry, and 2.1 wt% tetraethyl orthosilicate was then added into the slurry. The SiO_2 chemical coating on the powder surfaces was next caused by adjusting the pH using ammonia solution. Then the suspension was dried at $120\text{ }^\circ\text{C}$, and then calcined at $500\text{ }^\circ\text{C}$ for 4 hours to obtain the 0.6 wt% SiO_2 coated BTBZNT powders (BTBZNT@ SiO_2). The multilayer capacitors were prepared via tape casting method. The ceramic slurries for tape casting were

reported previously.⁸ The ceramic tapes screen-printed with 60Ag/40Pd paste as the internal electrodes were stacked layer by layer and precisely aligned using isostatic lamination with two active dielectric layers. Then, the MLCCs were sintered with the heating schedule as shown in fig. S6. Finally, silver paste was used to terminate the opposite ends of MLCCs for further electrical property measurements.

Characterizations: The crystal structures were characterized using X-ray diffraction (D8 Advance, Bruker, Karlsruhe, Germany) with CuK α radiation ($\lambda=1.5418$ Å). The microstructures of the MLCCs were observed by scanning electron microscope (MERLIN VP Compact, Carl Zeiss, Oberkochen, Germany). Dielectric properties over broad frequency and temperature were measured by an impedance analyzer (E4980A, Agilent Technologies Inc., Santa Clara, CA, USA). Ferroelectric and leakage properties were characterized with TF ANALYZER 2000E ferroelectric measurement system (aixACCT Systems GmbH, Aachen, Germany). The energy release properties of MLCCs were investigated by a charge-discharge platform (CFD-001, Gogo Instruments Technology, Shanghai, China) with a certain discharge resistance, and capacitance load circuit (RLC). HRTEM and EDS investigations were performed using field-emission transmission electron microscope (JEM-2010F and JEM-2100, JEOL Ltd., Tokyo, Japan), operating at 200 kV. The STEM experiments were performed using a spherical aberration-corrected Titan Themis TEM with a double tilting stage, operating at 300 kV, and the STEM detector was a high angle annular dark field (HAADF) detector with a camera length of 115 mm and the corresponding collection semi-angle range of 48 to 200 mrad. All the image filtering, peak finding, Gaussian

fitting, and statistic work were performed using the self-made MATLAB code.

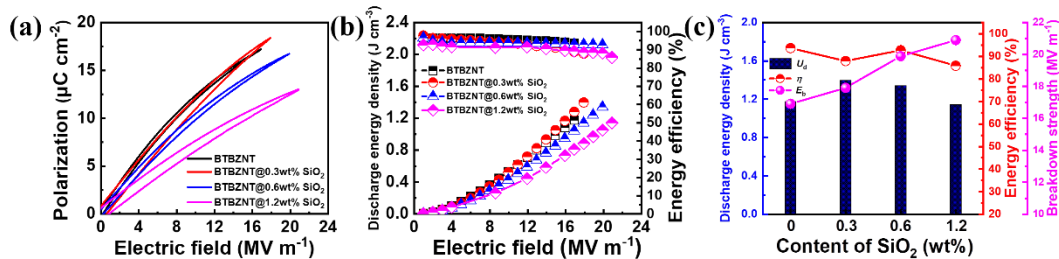


Figure S2 (a) P - E loops under maximum applied electric field of the BTBZNT@SiO₂ ceramics with different SiO₂ content measured at ambient temperature and 1 Hz. (b) The calculated U_d and η versus applied electric field for the BTBZNT@SiO₂ ceramics. (c) Energy storage properties of various BTBZNT@SiO₂ ceramics at room temperature.

0.87BaTiO₃-0.13Bi(Zn_{2/3}(Nb_{0.85}Ta_{0.15})_{1/3})O₃@SiO₂ powders with different SiO₂ content were prepared by chemical coating method. The ceramic samples for measuring energy storage properties were polished to a thickness of ~ 0.2 mm, and both sides were covered by Ag electrodes with a diameter of 3 mm. SiO₂ is linear dielectric materials with very low relative permittivity ($\epsilon_r \sim 4.5$) and high breakdown strength ($E_b \sim 1500$ MV m⁻¹).⁹ Therefore, the maximum polarization under same electric field of various BTBZNT@SiO₂ ceramics decreases with increasing SiO₂ content, while the breakdown strength increases. The optimal discharge energy density of 1.34 J cm⁻³ with a high energy efficiency of 92.7% is achieved at an electric field of 20 MV m⁻¹ for the BTBZNT@0.6wt% SiO₂ ceramics. The energy storage properties of various BTBZNT@SiO₂ ceramics are shown in Table S1. Comprehensively considering the energy storage properties of various BTBZNT@SiO₂ ceramics, we choose 0.6wt% SiO₂ composite material to prepare MLCCs.

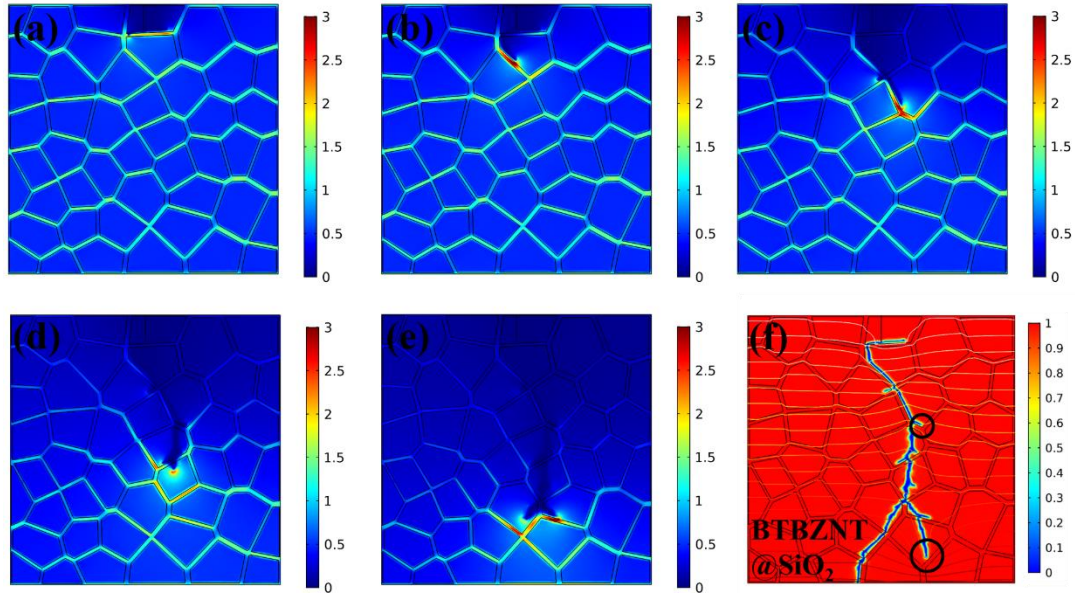


Figure S3 (a to e) The nominal electric field distribution at different moments during breakdown path growing. (f) Breakdown path image of BTBZNT@SiO₂ ceramics.

Generally, there is an approximate reciprocal relationship between the breakdown strength and the relative permittivity of dielectric materials ($E_b = 35\epsilon_r^{-0.64}$ MV cm⁻¹).⁹ Therefore, SiO₂ has a significantly higher breakdown strength than BaTiO₃-based ferroelectric and relaxor ferroelectric materials, and the electric field will concentrate in the SiO₂ layer (Figure S3a). In our composite system, the breakdown will be limited to the breakdown of the BTBZNT. The breakdown behavior will take priority in the BTBZNT. Under the applied electric field, breakdown will initiate from the weak areas (BTBZNT grains), and the electrical branches propagate in the BTBZNT grains (Figure S3a and b). When the breakdown path encounters SiO₂ layer, the growth of breakdown path will be inhibited, such as the black circled part in Figure S3b and f. Then, the breakdown path grows along the inside of the BTBZNT grain, where is close the SiO₂ layer. The electric field concentration will aggravate at the end of the growing breakdown path (Figure S3c). With the increase of the applied electric field, the local electric field exceed the breakdown strength of SiO₂ layer. Then the breakdown path will be through the SiO₂ layer (Figure S3c to e). When the breakdown path runs through the entire dielectric materials, including SiO₂ and BTBZNT, the MLCCs breakdown behavior occurs (Figure S3f). Overall, the SiO₂ layers with high breakdown energy will greatly enhance the breakdown strength of the composite dielectric materials.

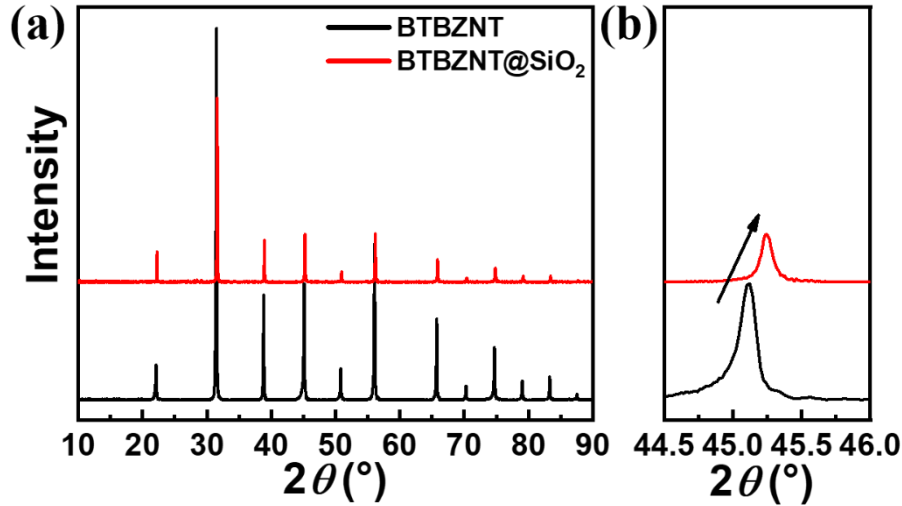


Figure S4 XRD patterns of the BTBZNT and BTBZNT@SiO₂ ceramics. (a) Theta-2theta from 10° to 90°. (b) Theta-2theta from 44.5° to 46.0°. All the ceramics are pure pseudocubic perovskite structures without any secondary phases. The content of SiO₂ in the BTBZNT@SiO₂ ceramics is only 0.6 wt%, which is too little to be detected by XRD. Therefore, there are no obvious diffraction peaks of the SiO₂ in the XRD result. Compared with the BTBZNT sample, the (200) peak of the BTBZNT@SiO₂ shifts to high angle, indicating a decreasing lattice parameter. Because of the smaller ionic mismatch, Si ions (0.40 Å, CN=6) more likely substitute on Ti sites (0.745 Å, CN=6) rather than Ba sites (1.61 Å, CN=12).¹⁰ The Si ions diffused into grain lattice substituted on Ti sites, making the diffraction peaks shift to high angle. On the other hand, the pressure stress due to the shell can also make the diffraction peaks shift to high angle.¹¹

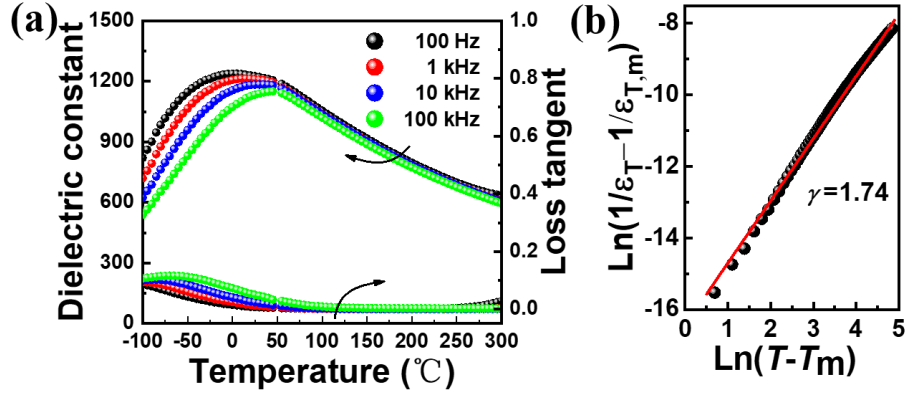


Figure S5 (a) Temperature-dependent dielectric constant and loss tangents of the BTBZNT@SiO₂ ceramics measured at various frequencies. (b) Fitting of the relaxor factor γ of BTBZNT@SiO₂ ceramics with the modified Curie-Weiss law at the frequency of 1 MHz. The dielectric characteristics of relaxor ferroelectric can be described by the modified Curie-Weiss law: $1/\varepsilon - 1/\varepsilon_m = (T - T_m)^\gamma/C$, where ε is the dielectric constant at temperature T , ε_m is the maximum value of dielectric constant, and T_m is the temperature corresponding to ε_m , C is the Curie constant, and γ is an indicator of the degree of diffuseness varying from 1 for a normal ferroelectric and 2 for an ideal relaxor ferroelectric.¹²

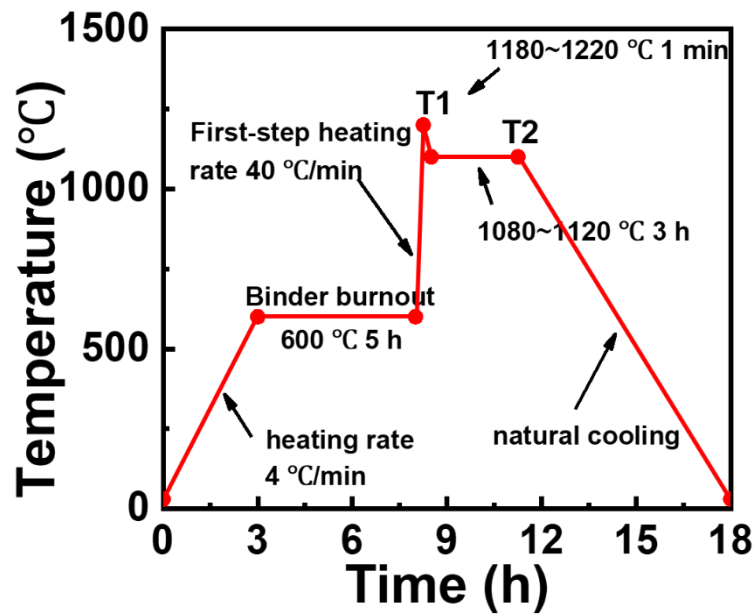


Figure S6 The two-step sintering heating schedule of MLCC. This two-step sintering method is a universal method for preparing nanocrystalline ceramics.^{8, 13} More importantly, the fast first-step heating rate will improve the interface bonding between the internal electrodes and dielectric layers. A good quality interface bonding also contributes to a low leakage current density, a high E_b , η , and thermal stability.¹⁴⁻¹⁶

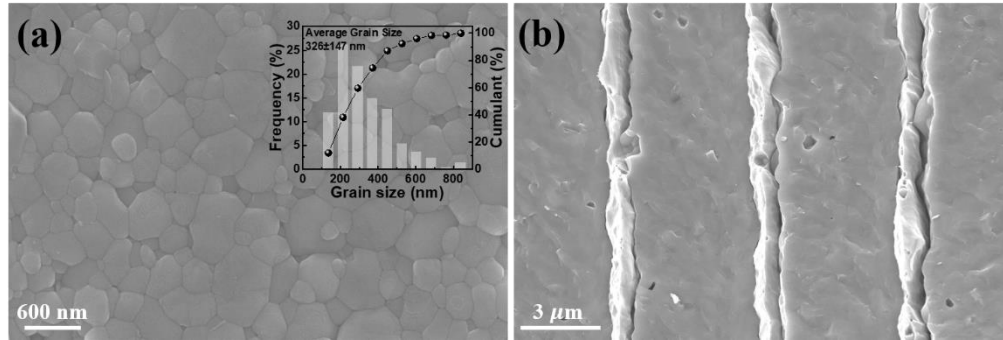


Figure S7 SEM images for the surface (a) and cross-section (b) of the BTBZNT@SiO₂ MLCC. The inset of (a) is the grain size distribution of the MLCC. After two-step sintering, the MLCC is found to possess fine grain with an average size of 326 nm. The nanograins will lead to a high E_b , η , and thermal stability.^{8, 17, 18} The images show the compact dielectric layer with continuous 60Ag/40Pd electrode layers, and the thickness of electrode layers and dielectric layers are about 1 μm and 4.7 μm , respectively.

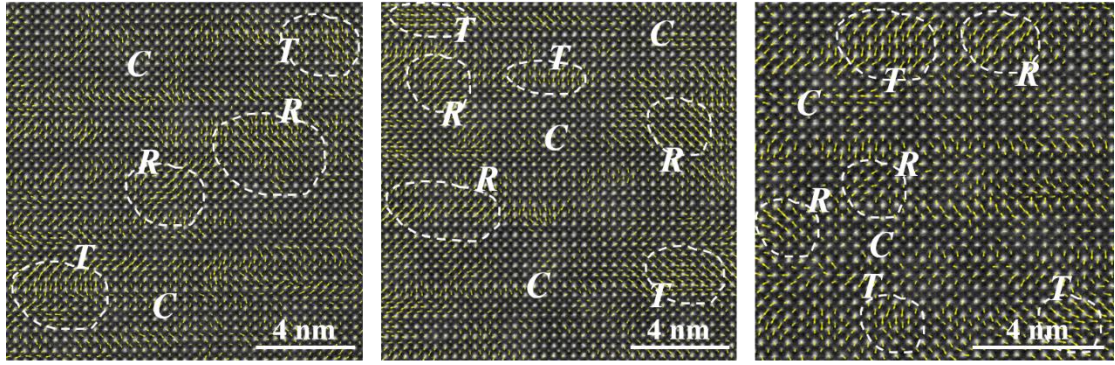


Figure S8 The HAADF STEM images and domain structures of the BTBZNT@SiO₂ MLCCs. The white dashed lines delineate the PNRs with the projected cation displacements denoted by yellow arrow.

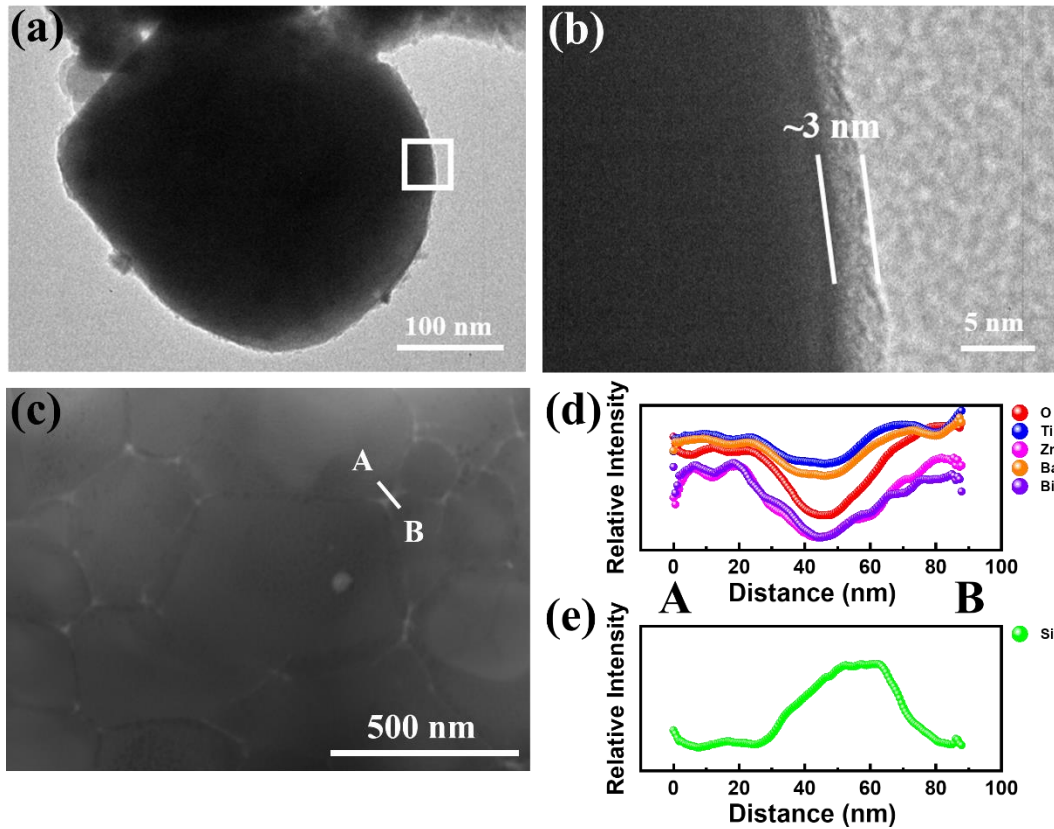


Figure S9 (a) Low-magnification and (b) high-magnification TEM bright-field images for BTBZNT@SiO₂ powders. (c) Low-magnification TEM bright-field image for BTBZNT@SiO₂ ceramics. (d and e) EDS line profiles of various elements distributions along the Line AB in (c). It can be easily found that the Si element is greatly enriched at the grain boundary from the EDS line profiles. The thickness of the SiO₂ layers in the ceramics is about 10~15 nm, indicating that some Si ions diffuse into grain lattice of BTBZNT shell during sintering process while most of Si elements segregated at the grain boundary. The Si-enriched areas have different contrast and exist around most grains. It is clearly found that the composite core-shell structure widely exists in our MLCC samples.

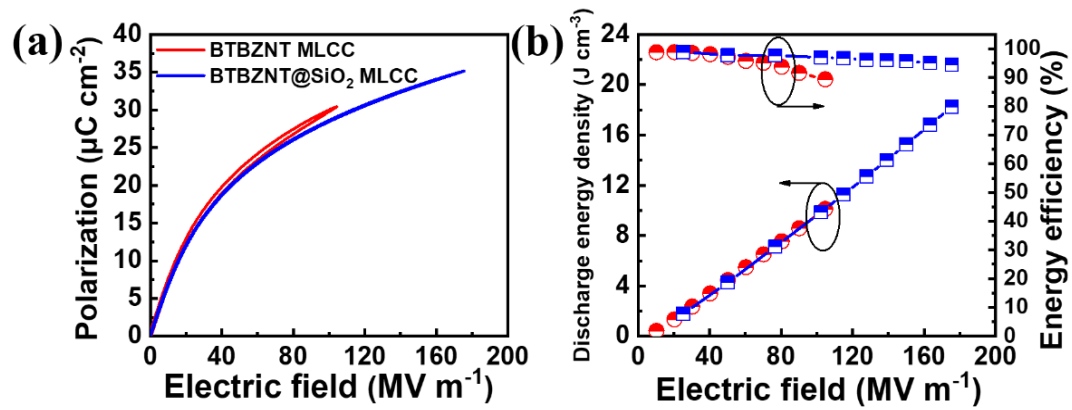


Figure S10 (a) Unipolar P - E loops under maximum applied electric field of BTBZNT and BTBZNT@SiO₂ MLCCs measured at room temperature and 10 Hz. (b) The calculated U_d and η versus applied electric field for the BTBZNT MLCCs and BTBZNT@SiO₂ MLCCs. Through multiscale optimization strategy, there is a remarkable enhancement on the energy storage performance in BTBZNT@SiO₂ MLCCs compared with our previous BTBZNT MLCCs, the E_b and U_d increased by 68% and 80%, respectively (see Table S2 for details).

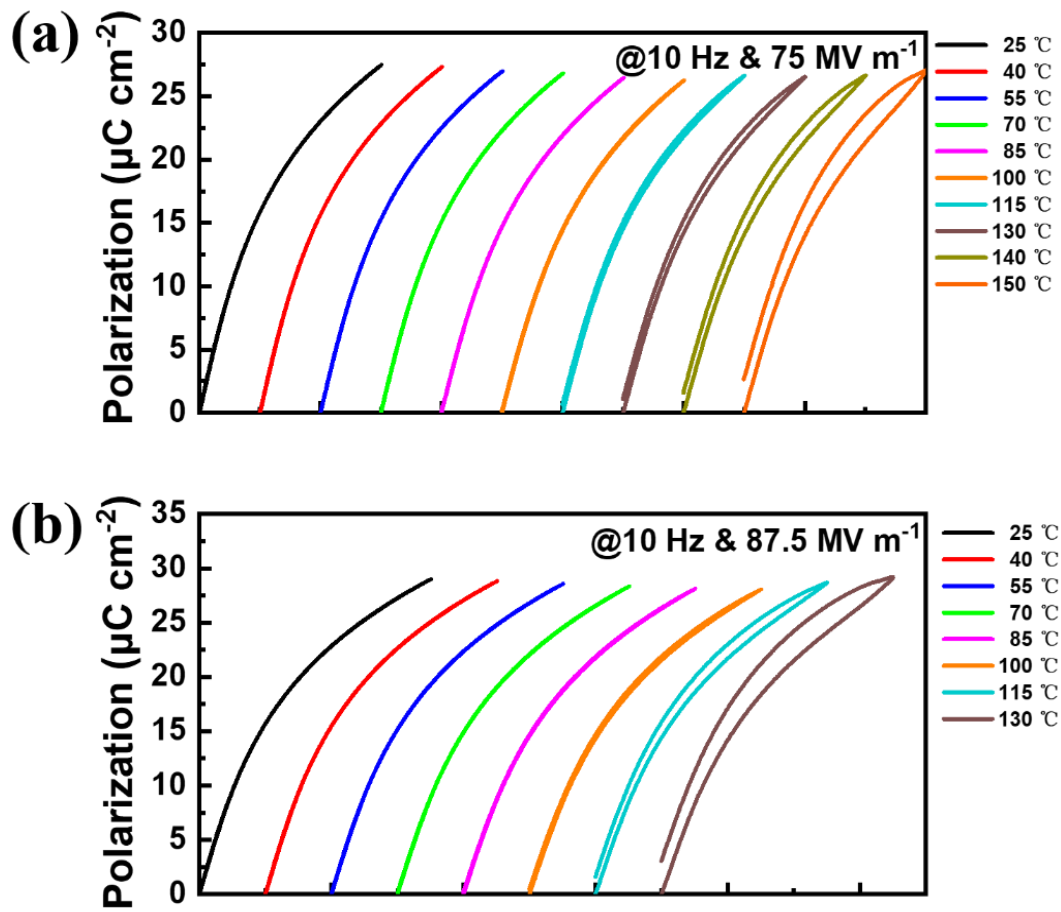


Figure S11 Unipolar $P-E$ loops of the BTBZNT@SiO₂ MLCCs at various temperature and applied electric field. (a) $E = 75 \text{ MV m}^{-1}$. (b) $E = 87.5 \text{ MV m}^{-1}$.

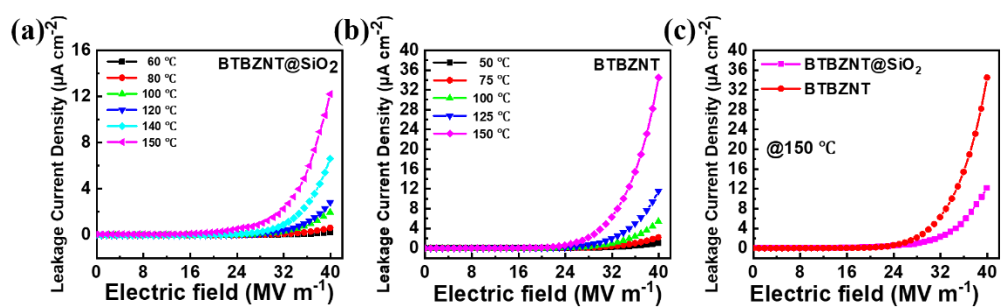


Figure S12 The leakage current density of the (a) BTBZNT@SiO₂, (b) BTBZNT MLCCs as a function of the applied electric field at various temperature, and (c) the comparison between the two samples at 150 °C.

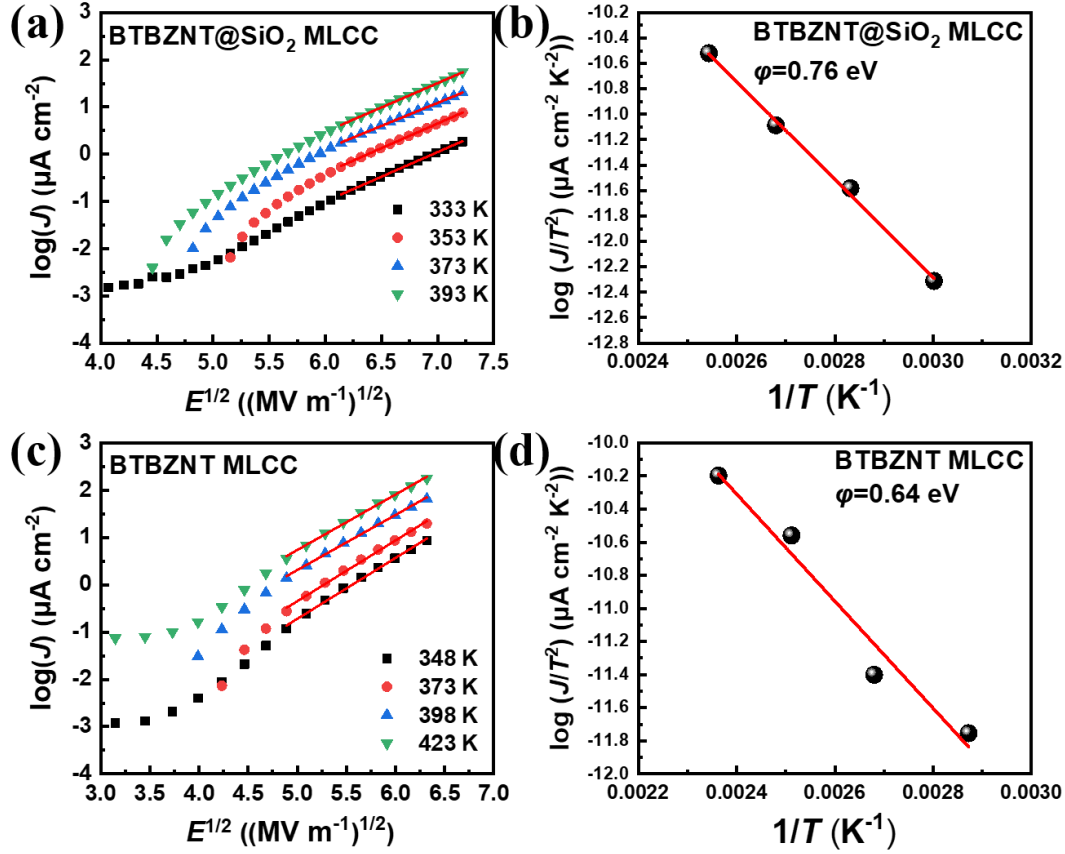


Figure S13 The Schottky thermionic emission model fitting of (a) BTBZNT@SiO₂ and (c) BTBZNT MLCC. (b) and (d) shows the Schottky barrier height fitting. The leakage current density (J) of the MLCCs is dependent on the thermodynamic temperature (T) and electric field (E). According to the Schottky emission model, the J is related to the Schottky barrier height,¹⁹ as described follow: $J = (4\pi eAk^2/h^3)T^2 \exp\left(\frac{-e\phi + \sqrt{e^3E/4\pi\epsilon_0\epsilon_r}}{kT}\right)$, where e is the effective electron mass, A is the effective Richardson constant, k is the Boltzmann constant, h is the Plank constant, ϕ is the Schottky barrier height, ϵ_0 is the vacuum permittivity, ϵ_r is the relative permittivity at optical frequency. Leakage current data in Figure S8 were adopted and linear correlations of $\log J$ and $E^{1/2}$ could be realized, guaranteeing the reliability of the Schottky thermionic emission model fitting results. The ϕ of the BTBZNT@SiO₂ and BTBZNT MLCC, evaluated from the plots of extrapolated values

of $\log J$ for $E \rightarrow 0$ versus $1/T$ in Figure S9B and S9C, were 0.76 and 0.64 eV, respectively. The Schottky barrier height can be approximated as the difference between the work function of the metal (φ_m) and the electron affinity of the ceramic (χ_c). The work function of alloy can be approximated by the Freeouf empirical model: $\varphi_{\text{alloy}} = \varphi_M^x \varphi_m^{1-x}$, where φ_M and φ_m are the work functions of metal M and m ($\varphi_{\text{Ag}} \sim 4.0$ eV, $\varphi_{\text{Pd}} \sim 5.55$ eV)²⁰, and x is the concentration of metal M.¹⁹ So the $\varphi_{60\text{Ag}/40\text{Pd}}$ is 4.56 eV. Assuming that the electron affinities of BTBZNT and BTBZNT@SiO₂ ceramics are similar to χ_{BaTiO_3} ($\chi_{\text{BaTiO}_3} \sim 3.9$ eV)¹⁹, the Schottky barrier height between the electrode and dielectric is estimated to be ~ 0.66 eV. The fitting results of the Schottky barrier heights of BTBZNT and BTBZNT@SiO₂ MLCC are close to this value, suggesting that the fitting results are reasonable.

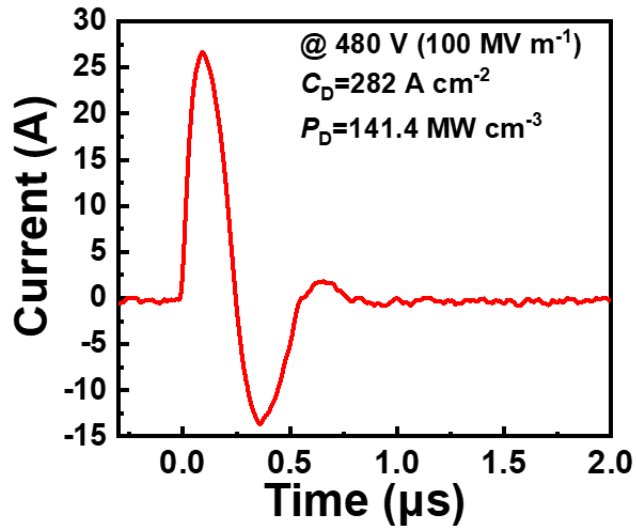


Figure S14 Undamped pulsed discharge current curve of BTBZNT@SiO₂ MLCCs at 100 MV m⁻¹.

The current density (C_D) and power density (P_D) can be calculated from the curve²¹: $C_D = I_{\max}/S$, $P_D = EI_{\max}/2S$, where I_{\max} , E , and S represent the maximum value of undamped pulsed discharge current curve, electric field, and electrode area, respectively. The P_D of BTBZNT@SiO₂ MLCCs under 100 MV m⁻¹ is about 141.4 MW cm⁻³, suggesting its high potential for pulsed power systems application.

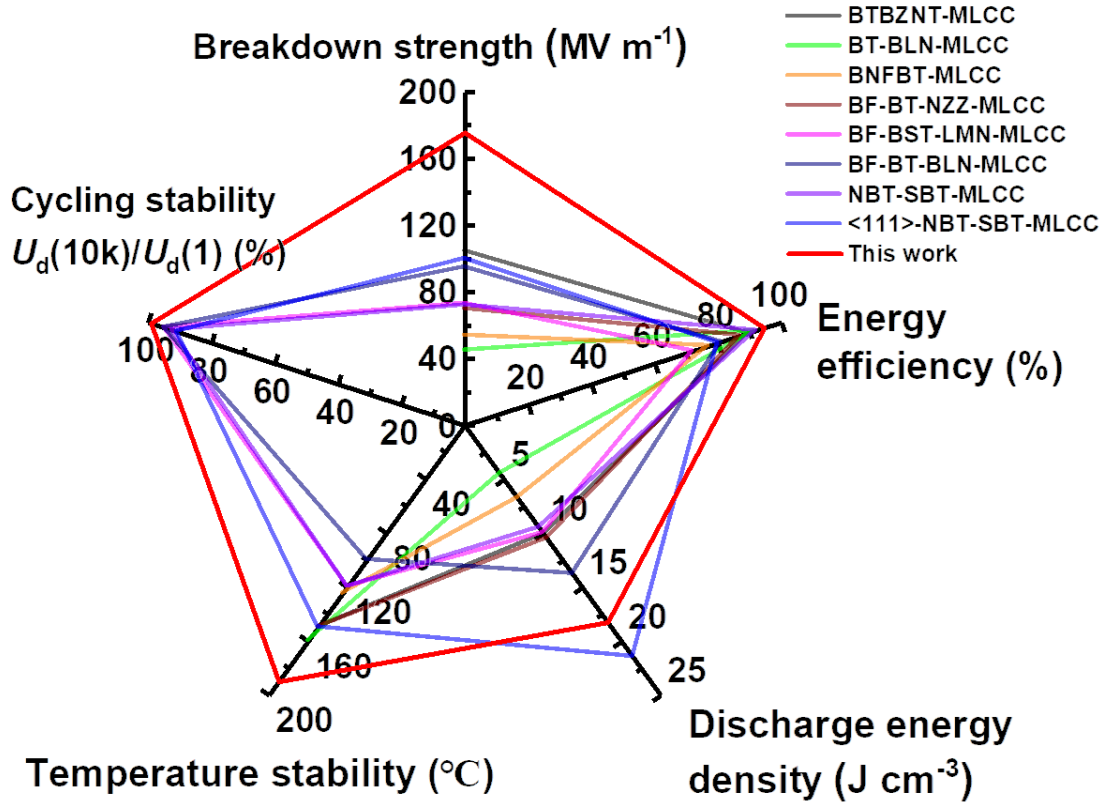


Figure S15 Comparison of the comprehensive energy storage performance (including the breakdown strength, energy efficiency and discharge energy density at maximum applied electric field, the temperature stability, and the cycling stability) for $0.87\text{BaTiO}_3\text{-}0.13\text{Bi}(\text{Zn}_{2/3}(\text{Nb}_{0.85}\text{Ta}_{0.15})_{1/3})\text{O}_3\text{@SiO}_2$ MLCCs and current state-of-the-art lead-free energy storage MLCCs. The temperature stability is expressed by the maximum reliable working temperatures of the MLCCs. The cycling stability is expressed by the ratio of the discharge energy densities after 10,000 cycles to the initial discharge energy densities of the MLCCs. The references of the energy storage MLCCs in legend can be found in the Table S3. The discharge energy density (18.24 J cm^{-3}) is by far the highest ever achieved in lead-free energy storage MLCCs (except recently reported <111>-textured NBT-SBT MLCCs,²² which are far more complicated to prepare and hard for scalable processing). The BTBZNT@SiO₂ MLCCs with low-cost

Ag/Pd internal electrode are feasible to prepare by the current well-developed MLCCs processing technology. Furthermore, the breakdown strength (175.5 MV m^{-1}), energy efficiency (over 94.5%), temperature stability (maximum reliable working temperature of $190 \text{ }^\circ\text{C}$), and cycling stability (variation $< 1\%$ after 10,000 cycles) are much more excellent than $\langle 111 \rangle$ -textured NBT-SBT MLCCs and other current MLCCs, demonstrating that the BTBZNT@SiO₂ MLCCs possess the superior comprehensive energy storage performance.

Table S1 Comparisons of various BTBZNT@SiO₂ ceramics

Content of SiO ₂ (wt%)	E_b (MV m ⁻¹)	U_d (J cm ⁻³)	η (%)
0	17	1.18	93.7
0.3	18	1.40	87.9
0.6	20	1.34	92.7
1.2	20.9	1.14	85.8

Table S2 Comparisons of BTBZNT and BTBZNT@SiO₂ energy storage MLCCs

Capacitor	Details	E_b (MV m ⁻¹)	U_d (J cm ⁻³)	η (%)
BTBZNT	2 dielectric layers with ~5 μ m	104.7	10.12	89.4
BTBZNT@SiO ₂	2 dielectric layers with ~5 μ m	175.5	18.24	94.5

Table S3 Energy storage performance of various MLCCs

	Composition	Internal electrode	E_b (MV m ⁻¹)	U_d (J cm ⁻³)	η (%)	Ref.
	BTBNT	60Ag/40Pd	45	2.76	84.3	23
BaTiO ₃ - based	BT-BLT	Pt	46.6	4.05	95.5	25
	BT-BLN	Pt	45	4.5	91.5	24
	BTBZNT	60Ag/40Pd	104.7	10.12	89.4	8
CaTiO ₃ - based	CTCH	Pt	120	9	93	26
	CTCH-Mn	Pt	130	9.6	96	26
PbTiO ₃ -based	PBLDZST	5Ag/95Pd	30	3.8	67.4	27
	BNF-BT	Pt	54	6.74	77	28
BiFeO ₃ - based	BF-BST-LMN	Pt	73	10	72	29
	BF-BT-NZZ	Pt	70	10.5	87	30
	BF-BT-BLN	Pt	95	13.8	81	31
(Bi _{0.5} Na _{0.5})Ti O ₃ -based	NBT-SBT	Pt	72	9.5	92	18
BTBZNT @SiO ₂		60Ag/40Pd	175.5	18.24	94.5	This work

Table S4 Comparisons of BTBZNT@SiO₂ MLCC and various commercial energy storage capacitors

Capacitor	Number	U_d (J cm ⁻³), 500 V	η (%)
BTBZNT@SiO ₂		9.88	97.0
PLZT-based AFE capacitor ³²	B5803115105 M002	0.69	89.5
BT-based RFE capacitor ³²	C1812C334K CRACTU	0.37	62.9
PP linear capacitor ³²	R75PI3330AA 30J	0.01	98.4

References

1. W. Hong and K. C. Pitike, *Procedia IUTAM*, 2015, **12**, 73-82.
2. Z. Cai, X. Wang, B. Luo, W. Hong, L. Wu and L. Li, *Composites Science and Technology*, 2017, **145**, 105-113.
3. K. C. Pitike and W. Hong, *Journal of Applied Physics*, 2014, **115**, 8.
4. J. Zhao, Z. Xu, G. Chen and P. L. Lewin, *J. Appl. Phys.*, 2010, **108**.
5. G. Chen and S. H. Loi, *MRS Proceedings*, 2011, **889**.
6. G. Chen, J. Zhao, S. Li and L. Zhong, *Appl. Phys. Lett.*, 2012, **100**.
7. S. Li, Y. Zhu, D. Min and G. Chen, *Sci. Rep.*, 2016, **6**, 32588.
8. P. Zhao, H. Wang, L. Wu, L. Chen, Z. Cai, L. Li and X. Wang, *Adv. Energy Mater.*, 2019, **9**, 1803048.
9. J. W. McPherson, K. Jinyoung, A. Shanware, H. Mogul and J. Rodriguez, *IEEE Transactions on Electron Devices*, 2003, **50**, 1771-1778.
10. R. D. Shannon, *Acta Cryst. A*, 1976, **32**, 751-767.
11. G. Yao, X. Wang, T. Sun and L. Li, *J. Am. Ceram. Soc.*, 2011, **94**, 3856-3862.
12. Z. Shen, X. Wang, B. Luo and L. Li, *J. Mater. Chem. A*, 2015, **3**, 18146-18153.
13. Chen I-W and W. XH, *Nature*, 2000, **404**, 168.
14. Z. Cai, C. Zhu, H. Wang, P. Zhao, L. Chen, L. Li and X. Wang, *J. Mater. Chem. A*, 2019, **7**, 14575-14582.
15. M. M. Samantaray, A. Gurav, E. C. Dickey and C. A. Randall, *J. Am. Ceram. Soc.*, 2012, **95**, 264-268.
16. M. M. Samantaray, A. Gurav, E. C. Dickey and C. A. Randall, *J. Am. Ceram. Soc.*, 2012, **95**, 257-263.
17. Z. Cai, X. Wang, W. Hong, B. Luo, Q. Zhao and L. Li, *J. Am. Ceram. Soc.*, 2018, **101**, 5487-5496.
18. J. Li, F. Li, Z. Xu and S. Zhang, *Adv Mater*, 2018, **30**, 1802155.
19. A. V. Polotai, I. Fujii, D. P. Shay, G.-Y. Yang, E. C. Dickey and C. A. Randall, *J. Am. Ceram. Soc.*, 2008, **91**, 2540-2544.
20. D. E. Eastman, *Phys. Rev. B*, 1970, **2**, 1-2.
21. X. Qiao, F. Zhang, D. Wu, B. Chen, X. Zhao, Z. Peng, X. Ren, P. Liang, X. Chao and Z. Yang, *Chemical Engineering Journal*, 2020, **388**.
22. J. Li, Z. Shen, X. Chen, S. Yang, W. Zhou, M. Wang, L. Wang, Q. Kou, Y. Liu, Q. Li, Z. Xu, Y. Chang, S. Zhang and F. Li, *Nat Mater*, 2020, **19**, 999-1005.
23. L. Chen, H. Wang, P. Zhao, C. Zhu, Z. Cai, Z. Cen, L. Li and X. Wang, *J. Am. Ceram. Soc.*, 2019, **102**, 4178-4187.
24. W.-B. Li, D. Zhou, R. Xu, L.-X. Pang and I. M. Reaney, *ACS Appl. Energy Mater.*, 2018, **1**, 5016-5023.
25. W. Li, D. Zhou, R. Xu, D.-W. Wang, J. Su, L.-X. Pang, W. Liu and G.-H. Chen, *ACS Appl. Energy Mater.*, 2019, **2**, 5499-5506.
26. D. P. Shay, N. J. Podraza, N. J. Donnelly and C. A. Randall, *J. Am. Ceram. Soc.*, 2012, **95**, 1348-1355.
27. L. Chen, N. Sun, Y. Li, Q. zhang, L. Zhang and X. Hao, *J. Am. Ceram. Soc.*, 2018, **101**, 2313-2320.

28. D. Wang, Z. Fan, D. Zhou, A. Khesro, S. Murakami, A. Feteira, Q. Zhao, X. Tan and Ian M. Reaney, *J. Mater. Chem. A*, 2018, **6**, 4133-4144.
29. G. Wang, Z. Lu, J. Li, H. Ji, H. Yang, L. Li, S. Sun, A. Feteira, H. Yang, R. Zuo, D. Wang and I. M. Reaney, *J. Eur. Ceram. Soc.*, 2020, **40**, 1779-1783.
30. G. Wang, J. Li, X. Zhang, Z. Fan, F. Yang, A. Feteira, D. Zhou, D. C. Sinclair, T. Ma, X. Tan, D. Wang and I. M. Reaney, *Energy Environ. Sci.*, 2019, **12**, 582-588.
31. G. Wang, Z. Lu, H. Yang, H. Ji, A. Mostaed, L. Li, Y. Wei, A. Feteira, S. Sun, D. C. Sinclair, D. Wang and I. M. Reaney, *J. Mater. Chem. A*, 2020, **8**, 11414-11423.
32. R. Xu, Y. Feng, X. Wei and Z. Xu, *IEEE Transactions on Dielectrics and Electrical Insulation*, 2019, **26**, 2005-2011.